Supporting information

Photothermal-Stable Flexible Perovskite Solar Cells Enabled by PbI_2 Suppression with Amino-Functionalized Graphene Quantum Dots

Hao Wang, Xiaoran Li, Wei Yu, and Xin Li*

School of Electronic Science and Engineering, Xiamen University, Xiamen 361005, China

Corresponding Author: *
Email: lixin01@xmu.edu.cn (Prof. Xin Li)

Materials

Methylammonium bromide (MABr, 99.8%) and formamidinium iodide (FAI, 99.9%) were purchased from Great Cell Solar Materials Pty Ltd (Australia). Lead iodide (PbI_2, 99.99%) and (4-(3,6-Dimethoxy-9H-carbazol-9-yl)butyl)phosphonic acid (MeO-4PACz) were purchased from TCI Co. Ltd. Cesium iodide (CsI, 99.999%), PCBM (99.9%) were purchased from Advanced Election Technology (China). Bathocuproine (BCP, 99%) was obtained from Xi'an Polymer Light Co. Ltd. Amino graphene quantum dots (A-GQDs) were purchased from Jiangsu Xianfeng nano material technology Co. Ltd. The PET/ITO flexible substrates were bought from Peccell (Japan). N, N-dimethylformamide (DMF, 99.8%), anisole (Ani, 99.7%), dimethyl sulfoxide (DMSO, 99.8%), chlorobenzene (CB, 99.8%), and isopropanol alcohol (IPA, 99.5%) were bought from Sigma-Aldrich.

Preparation of Precursor Solutions

The synthesis and purification of NiO_x nanopowders were carried out according to our previously described method [1]. The NiO_x ink was subsequently prepared by dispersing 20 mg of the resulting powder in 1 mL of deionized water.

Self-assembled monolayer (SAM) solutions were obtained by dissolving MeO-4PACz in IPA at a concentration of 1.0 mM.

To obtain perovskite with the composition $Cs_{0.05}(FA_{0.92}MA_{0.08})_{0.95}Pb(I_{0.92}Br_{0.08})_3$ of 1.55 eV, the 1.5 M precursor solution was prepared. The solution was made by dissolving the constituent salts (CsI, FAI, MABr, and PbI_2) in a 4:1 (v/v) mixture of DMF (800 μL) and DMSO (200 μL).

The A-GQDs solution was prepared by dissolving 1 mg A-GQDs in 1 mL of IPA.

The PCBM ink was obtained by dispersing 20 mg of PCBM in 1 mL of CB, while the BCP solution was made by dissolving 0.5 mg of BCP in 1 mL of IPA.

Flexible Perovskite Solar Cells (FPSCs) Fabrication

The 2 cm × 2 cm PET/ITO flexible substrates were rinsed successively with deionized water, ethanol, and isopropanol in an ultrasonic bath for 15 min per solvent. After being dried at 75 °C for 20 min, the substrates were treated with ultraviolet (UV)-ozone plasma for 20 min prior to the deposition of the NiO_x layer. The NiO_x layer was deposited onto the flexible substrates by spin-coating at 3000 rpm for 30s, followed by annealing at 120 °C for 15 min, yielding a thickness of approximately 30 nm. After cooling, the samples were transferred into an N_2-filled glovebox. The MeO-4PACz solution was then dynamically spin-coated onto the NiO_x film at 3000 rpm for 30 s, and the substrates were subsequently annealed at 100 °C for 10 min.

The perovskite layer was fabricated using a two-step spin-coating process: first at 1500 rpm for 10 s, followed by 6000 rpm for 25 s. Five seconds before the end of the second step, 200 μL of anisole was rapidly dripped onto the spinning substrate as an anti-solvent. Subsequently, the PCBM solution was spin-coated onto the perovskite layer at 2000 rpm for 30 s. Then, BCP solution in isopropanol was dynamically spin-

coated onto the PCBM layer at 6000 rpm for 30 s to complete the electron transport bilayer. Finally, silver electrode (100 nm) was subsequently deposited by a vacuum thermal depositing system.

Measurement and Characterization.

The photovoltaic performance of the flexible PSCs was characterized by recording photocurrent density-voltage (*J-V*) curves (Keithley 2400 source meter) under standard AM 1.5G illumination (100 mW cm^{-2}, Newport Oriel 94023A, USA). Measurements were performed in both reverse (1.2 V to -0.2 V) and forward (-0.2 V to 1.2 V) scan directions, with the light intensity calibrated against a certified silicon reference cell prior to testing. The device active areas were defined as 0.062 and 1.02 cm^2 using two stainless steel apertures. External quantum efficiency (EQE) spectra were recorded using a commercial system (QE-R-3010, Enlitech Technology, Taiwan) over a wavelength range of 300–900 nm with a 5 nm step interval.

Transmission electron microscope (TEM) and high-resolution transmission electron microscope (HRTEM) were measured by JEOL JEM-F200 (Japan). Structural characterization was conducted via X-ray diffraction (XRD) on a Rigaku Ultima-IV diffractometer (Japan). Grazing-incidence X-ray diffraction (GIXRD, Bruker D8 Advance) was employed to analyze the residual strain within the perovskite films. The surface morphologies of the perovskite films were examined using atomic force microscopy (AFM, Cypher ES) and scanning electron microscopy (SEM, SUPRA 55, Zeiss, Germany).

Optical and photophysical properties were investigated using several techniques. Steady-state photoluminescence (PL), time-resolved PL (TRPL), and PL quantum yield (PLQY) were measured on a fluorescence spectrometer (FLS1000, Edinburgh Instruments, UK) with a 468 nm excitation source. PL mapping was acquired using two complementary systems: a confocal Raman microscope (LabRAM HR Evolution, HORIBA France) and a Vis–NIR–XU instrument (Nanophoton Corporation) under the same excitation wavelength of 468 nm. Transmittance spectra were obtained using a UV-vis spectrophotometer (Cary 5000, USA) across the 300–900 nm range.

Chemical composition and electronic properties were probed by X-ray photoelectron spectroscopy (XPS) and ultraviolet photoelectron spectroscopy (UPS) on an ESCALAB 250XL system (Thermo Fisher Scientific, USA). All XPS spectra were calibrated by setting the binding energy of the C 1s peak to 284.8 eV.

Finally, the operational stability of the flexible devices was assessed under continuous illumination from a white LED array (OSRAM, Germany) calibrated to 100 mW cm^{-2}.

Supplementary Note 1

Calculation of the residual stress:

The residual stress σ can be calculated by the Equation (1):

$$\sigma = -\frac{E}{2(1+\upsilon)}\frac{\pi}{180^\circ}cot\theta_0\frac{\partial(2\theta)}{\partial sin^2\psi} \quad (1)$$

Given that the perovskite modulus (E) is 11.45 GPa, the Poisson's ratio (υ) is 0.3, and the stress-free diffraction angle ($2\theta_0$) is 31.665°, the residual strain in the perovskite film can be quantitatively estimated from the slope of the 2θ-sin²ψ linear fit.

Supplementary Note 2

Calculation of Trap densities:

The trap densities is quantitatively calculated by the following equation:

$$N_t = \frac{2\varepsilon\varepsilon_0 V_{TFL}}{qL^2} \quad (2)$$

Where the trap filling limit voltage (V_{TFL}) obtained from the SCLC curve, q is the basic charge, L is the thickness of the perovskite film, ε is the relative dielectric constant of perovskite, and ε_0 is the vacuum dielectric constant.

Supplementary Note 3

For high-performance perovskite solar cells, the FF is governed by non-radiative and charge transport losses. The theoretical maximum FF (FF_{max}) is given by the equation shown:

$$V_{oc} = \frac{qV_{oc}}{nK_BT/q} \tag{3}$$

$$FF_{max} = \frac{V_{oc} - \ln(V_{oc} + 0.72)}{V_{oc} + 1} \tag{4}$$

Here, n denotes the ideality factor, K_B is Boltzmann's constant, T is the temperature, and q is the elementary charge. The corresponding n values, derived from the semilogarithmic plot of V_{oc}versus light intensity (Figure 4h), were used in this calculation.

Supplementary Note 4

The Fermi energy (E_F) can be calculated from the following formula:

$$E_F = 21.22\ eV - E_{cutoff} \tag{5}$$

Where E_{cutoff} represents the cutoff of the UPS spectrum at the high binding energy range. In addition, the position of the valence band (VB) with respect to the Fermi level is determined from the low-energy tail of the UPS spectrum.

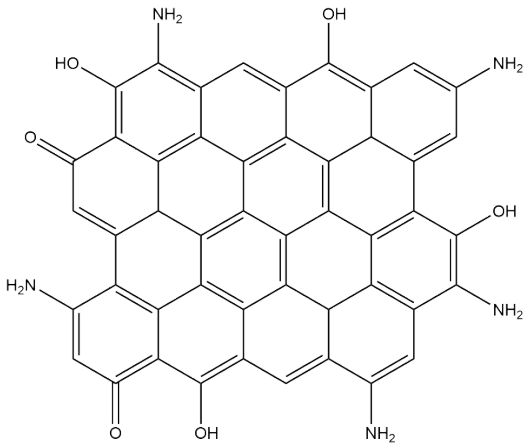

Figure S1. The structure schematic of Amino graphene quantum dots (A-GQDs).

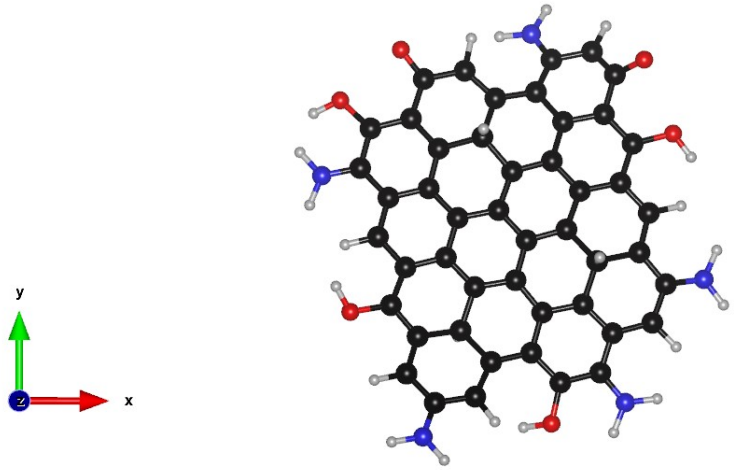

Figure S2. The simplified model of A-GQDs in the z-direction.

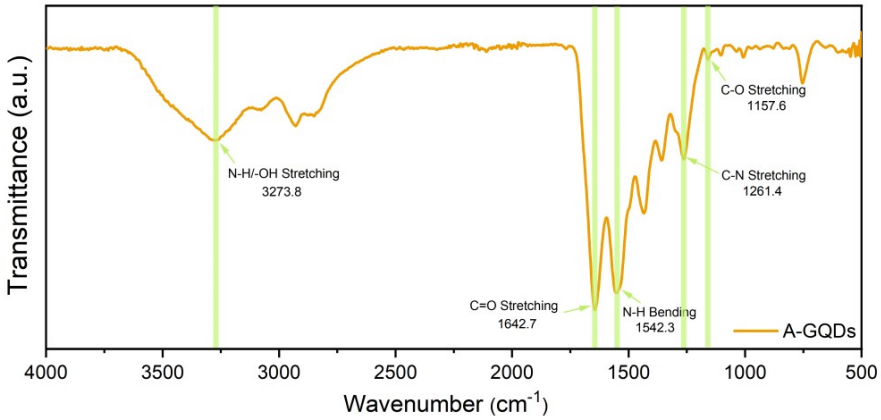

Figure S3. FT-IR spectra of A-GQDs, showing the signals of functional groups including N-H/-OH stretching, C=O stretching, N-H bending, C-N stretching, and C-O stretching vibration peaks.

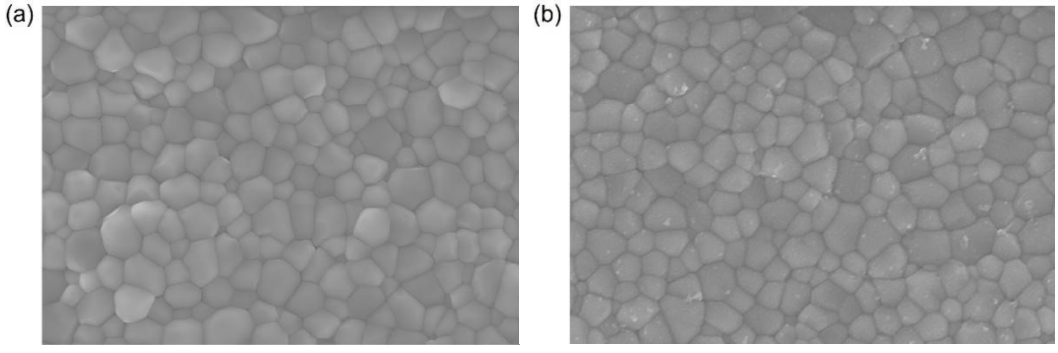

Figure S4. Top-view SEM images of perovskite films (a) without and (b) with A-GQDs modified at 30k magnification.

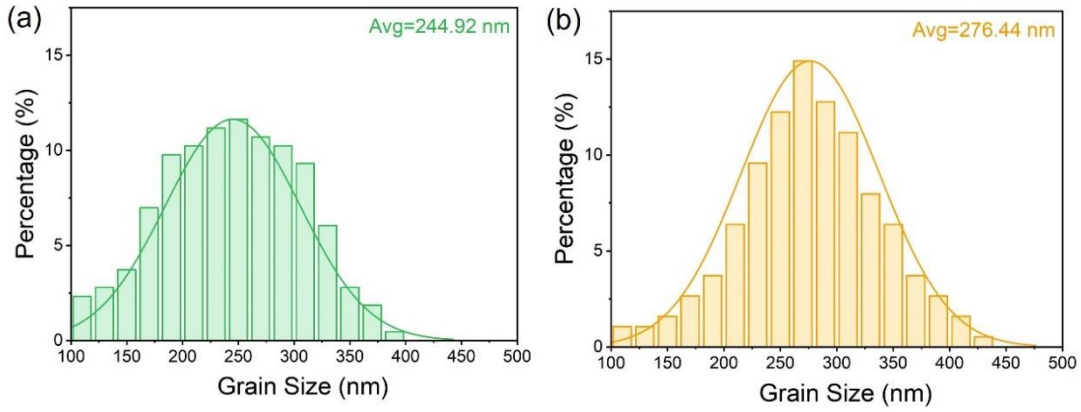

Figure S5. Histogram of grain size distribution corresponding to the top-view SEM of perovskite films (a) without and (b) with A-GQDs modified.

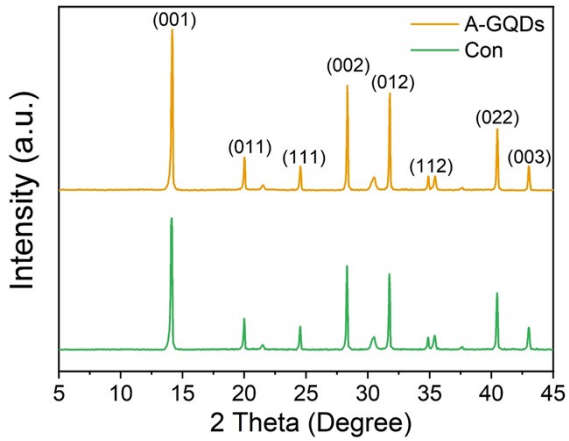

Figure S6. XRD patterns of control and A-GQDs modified perovskite films.

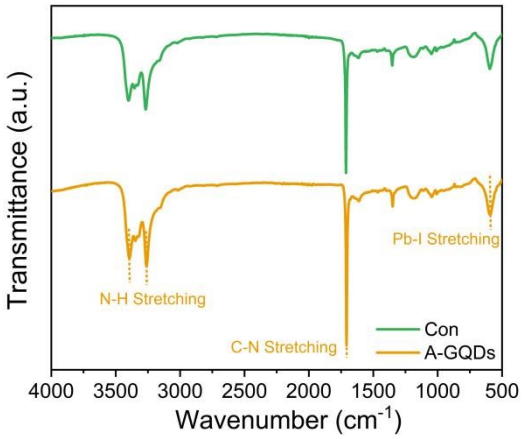

Figure S7. FTIR spectrum of control and A-GQDs modified perovskite films.

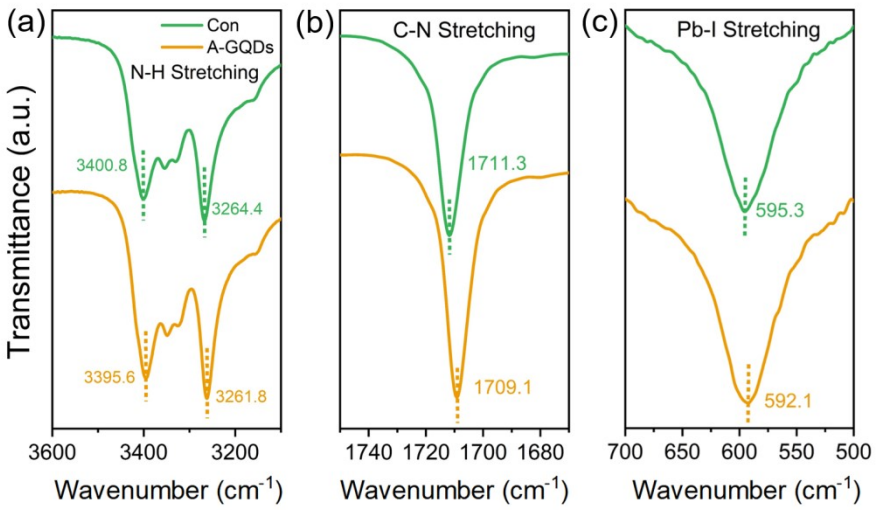

Figure S8. FTIR spectrum of control and A-GQDs modified perovskite films in specific vibrations.

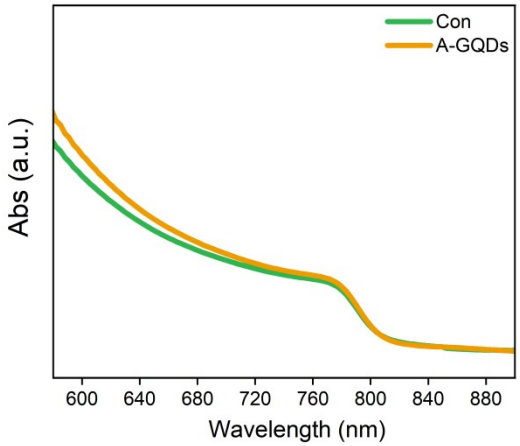

Figure S9. UV visible absorption spectroscopy of the control and A-GQDs modified perovskite films.

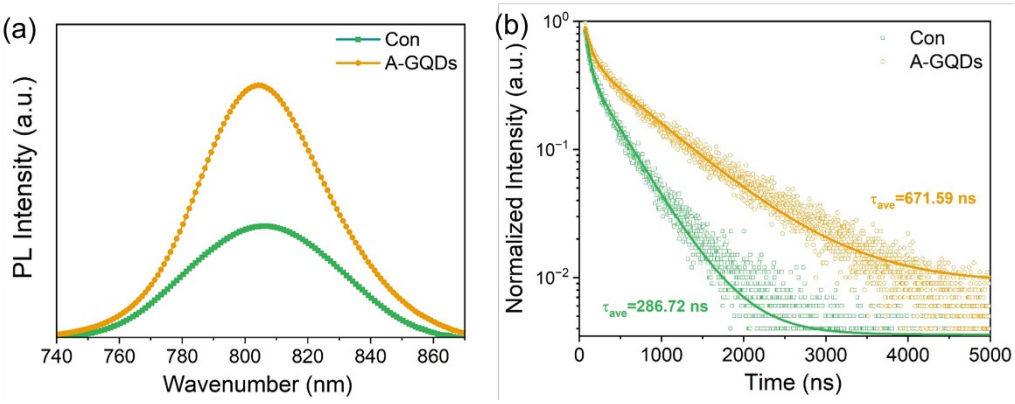

Figure S10. (a) Steady-state PL and (b) TRPL spectra of perovskite films without and with A-GQDs treatment.

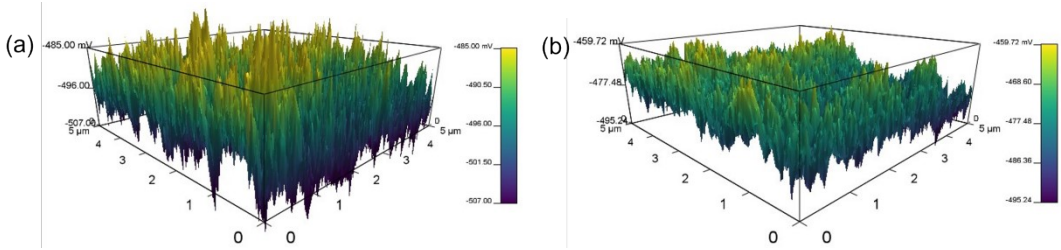

Figure S11. 3D KPFM images of (a) control and (b) A-GQDs modified perovskite films.

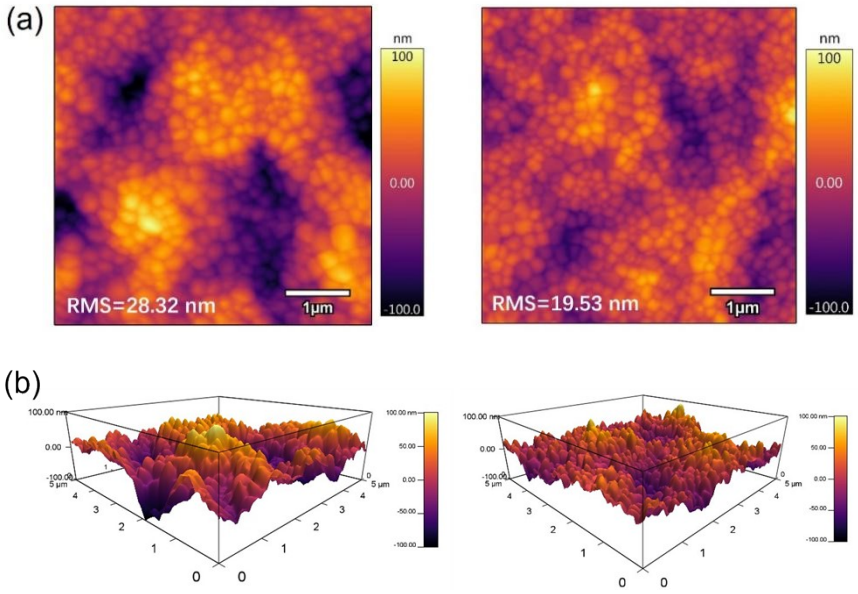

Figure S12. (a) AFM images of the perovskite films without and with A-GQDs treated, and (b) the corresponding 3D AFM images.

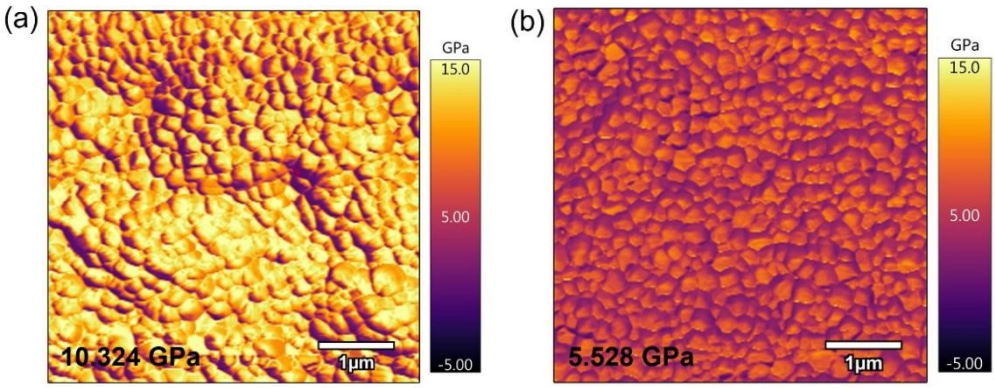

Figure S13. The images of Young's modulus of (a) control and (b) A-GQDs modified films, and the corresponding values are extracted from the AFM peak-force model.

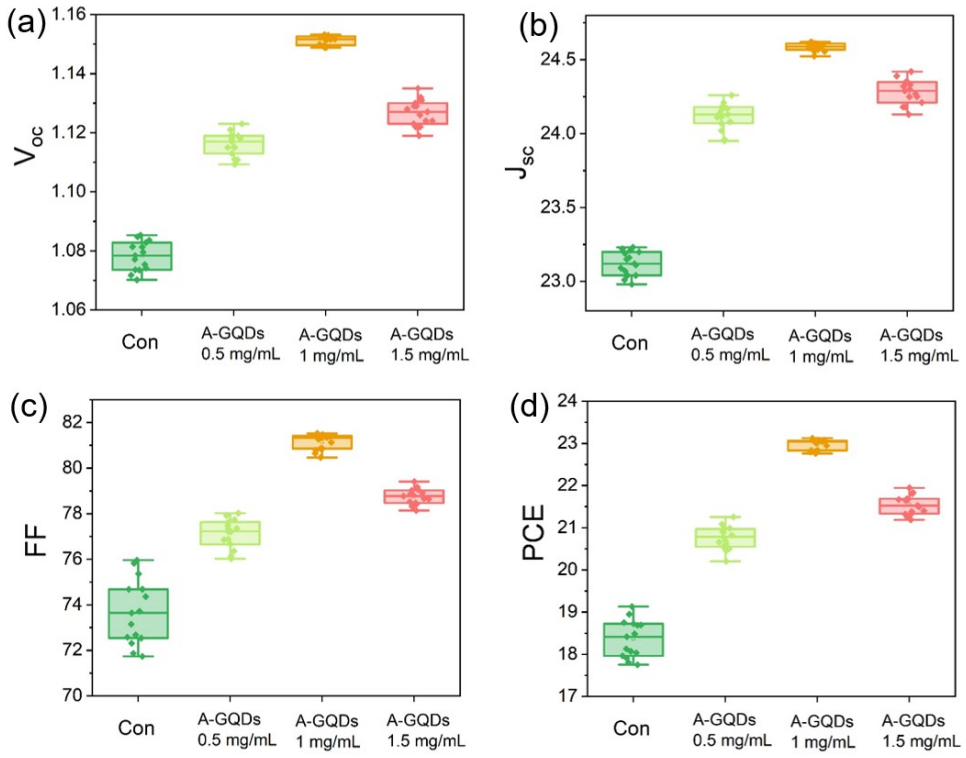

Figure S14. The dependence of photovoltaic parameters (a) V_{OC}, (b) J_{SC}, (c) FF and (d) PCE based on different concentration of A-GQDs.

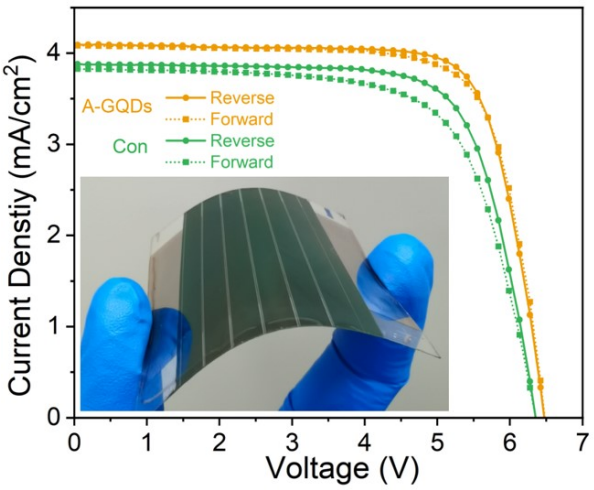

Figure S15. *J-V* curves of both reverse and forward scans of control and A-GQDs optimized flexible perovskite solar modules.

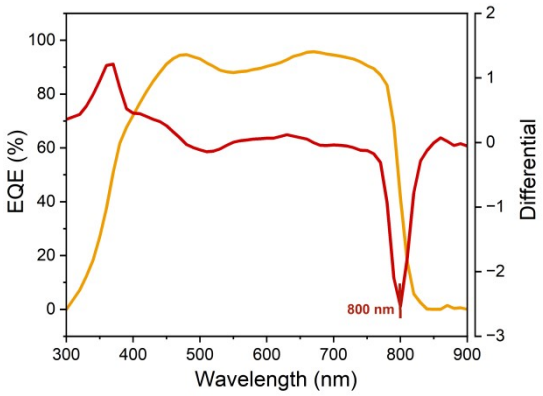

Figure S16. EQE and d(EQE)/dE versus wavelength of A-GQDs optimized FPSCs confirming the bandgap of 1.55 eV.

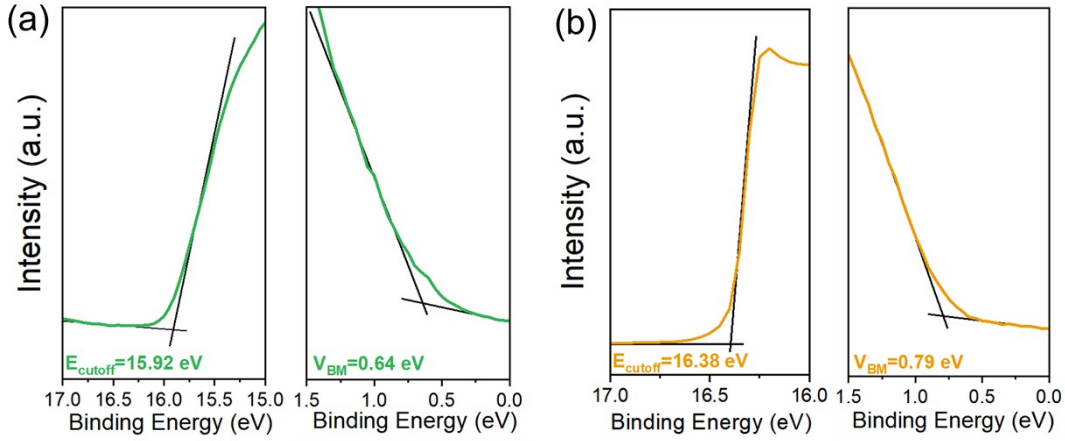

Figure S17. UPS spectra of perovskite films without and with A-GQDs modified.

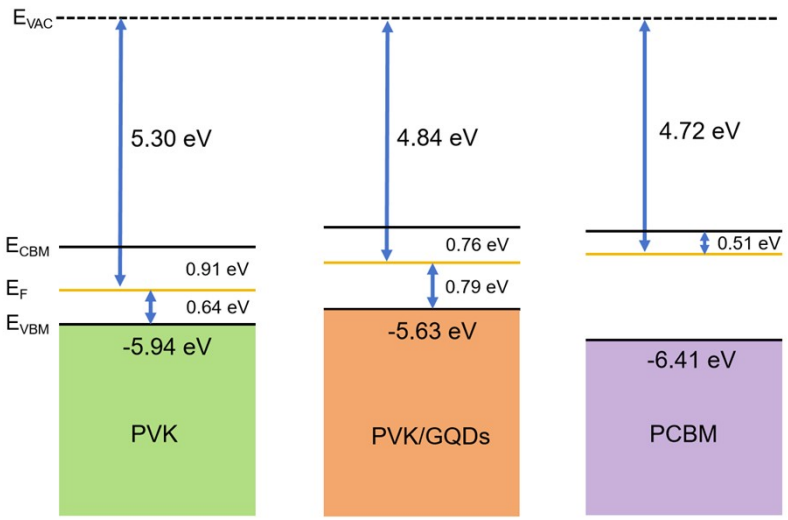

Figure S18. The energetic diagrams of the perovskite films without and with A-GQDs

treated based on values from UPS measurements referenced to the vacuum level.

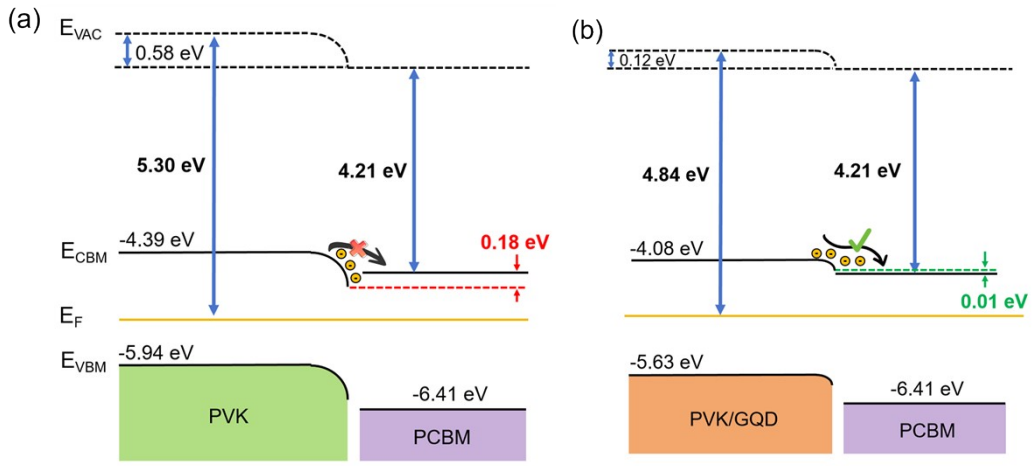

Figure S19. Energy-level diagrams of (a) control perovskite and PCBM, (b) A-GQDs modified perovskite and PCBM.

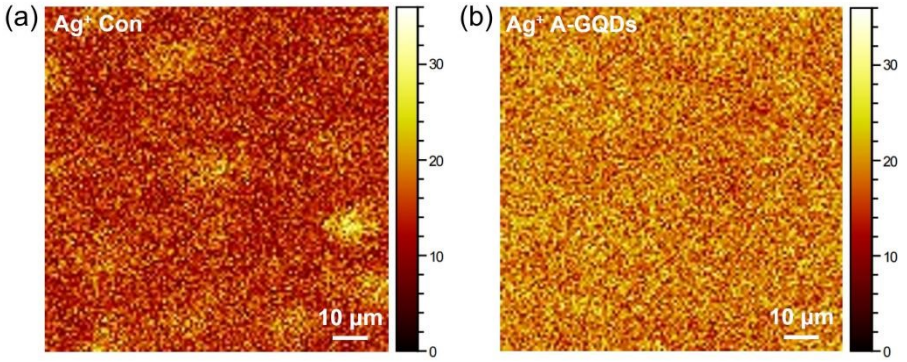

Figure S20. TOF-SIMS 2D surface mappings of Ag^+ for control and A-GQDs modified FPSCs.

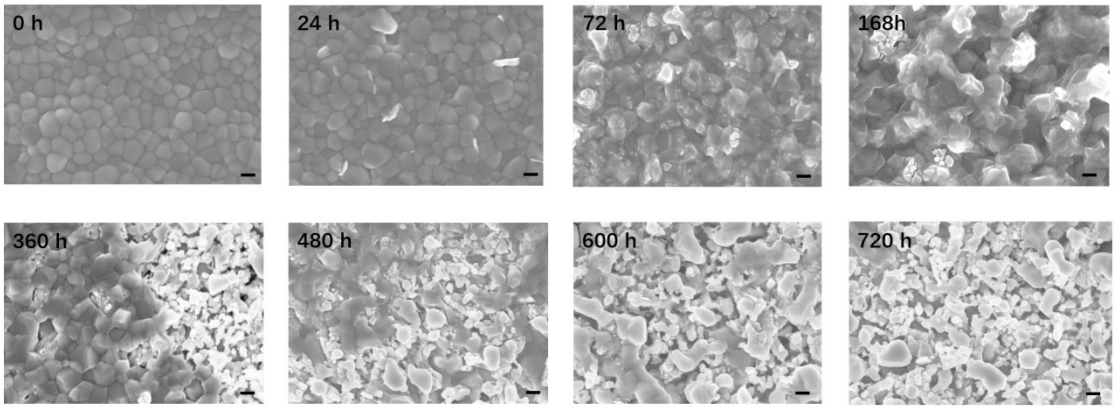

Figure S21. The aging SEM images of control perovskite film at different times from

0 h to 720 h under continuous 1 sun illumination and 85℃ heating.

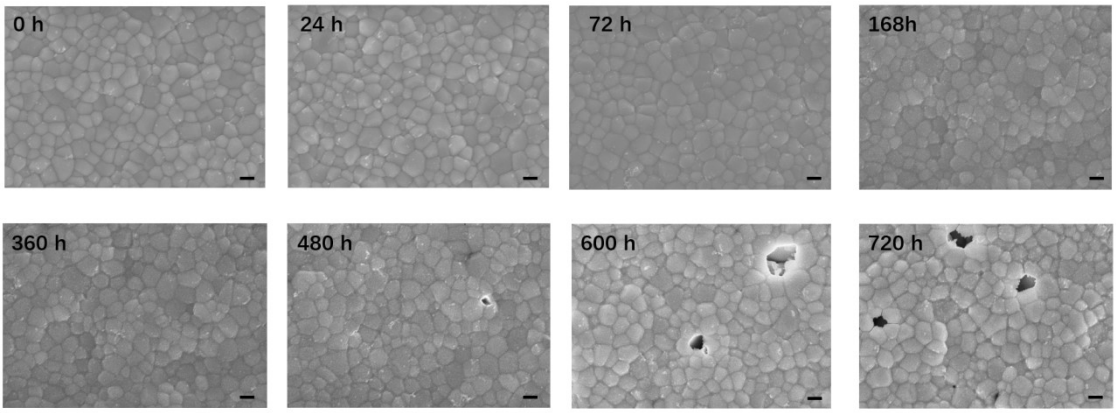

Figure S22. The aging SEM images of A-GQDs treated perovskite film at different times from 0 h to 720 h under continuous 1 sun illumination and 85℃ heating.

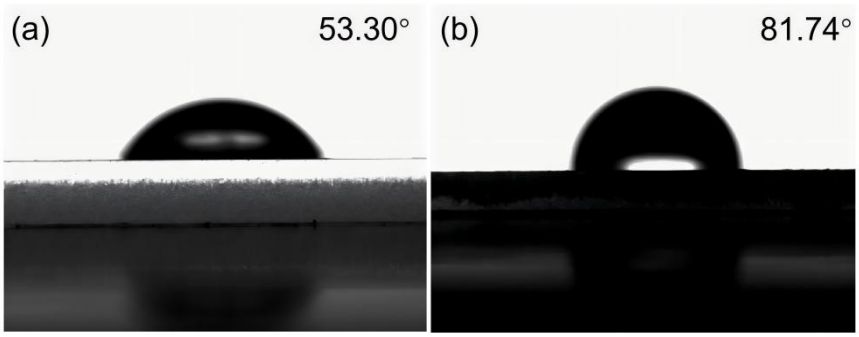

Figure S23. Water contact angles of perovskite films (a) without and (b) with A-GQDs treatment.

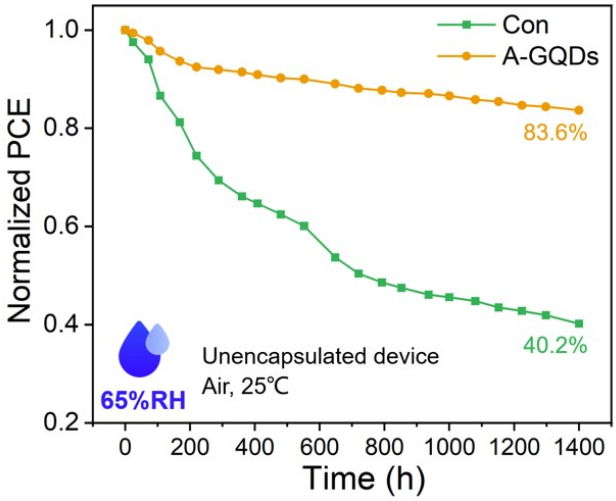

Figure S24. The environmental stability of unencapsulated FPSCs at 65% RH in

atmospheric environment.

Table S1. Comparison between previous GQDs-related studies and this work in PSCs.

Cell Type	Graphene type	Function Location	Device structure	Efficiency	Stability
Rigid n-i-p[2]	F/N co-doped graphene quantum dots (F/N-GQDs)	Additive of PVK antisolvent/ PVK interface	FTO/SnO_2/PVK(F/N-GQDs)/carbon electrode (CE)	16.37 %	90.1% of initial PCE, 1 sun illumination at the MPP, 100 h
Rigid /Flexible n-i-p[3]	GQD and SnO_2 nanoparticle composites (G@SnO_2)	G@SnO_2 ETLs	FTO(ITO/PEN)/G@SnO_2/PVK /Spiro-OMeTAD/Ag	19.6 % (Rigid) 17.7 % (Flexible)	91% of initial PCE, 500 bending cycles, 7 mm bending radius
Rigid n-i-p[4]	GQDs	SnO_2/PVK interface	ITO/SnO_2:GQDs/PVK/Spiro-OMeTAD/Au	20.23 %	95% of initial PCE, dark storage, 90 days
Rigid n-i-p[5]	GQDs	SnO_2/PVK interface	ITO/SnO_2:GQDs/PVK/Spiro-OMeTAD/Au	21.1%	80% of initial PCE, RH ≤ 30%, ambient air, 30 days
Rigid n-i-p[6]	Imidazole-graphene quantum dots (GQDs)	SnO_2/PVK interface	ITO/SnO_2/I-GQDs/PVK /Spiro-OMeTAD/Ag	22.37 %	84% of initial PCE, full-sun illumination, N_2, 600 h
Rigid n-i-p[7]	Fluorinated graphene quantum dots (F-GQDs)	Additive of PVK antisolvent	FTO/SnO_2/PVK (FGQDs)/Spiro-OMeTAD/Au	24.12 %	85% of initial PCE, dark storage, 30 days
Rigid p-i-n[8]	Fluorine functionalized graphene nanoplatelets (EFGnPs-F)	PCBM/Al interface	ITO/PEDOT:PSS/PVK/ PCBM/EFGnPs-F/Al	14.3%	82% of initial PCE, RH≈50%, 30 days

Rigid p-i-n[9]	nitrogen functionalized GQDs (NGQDs)	PVK/PCBM interface	ITO/NiO:Cu/PVK/NGQDs/PCBM/Ag	17.1%	Not mentioned
Rigid p-i-n[10]	Graphite-N (GN) GQDs	PVK precursor additive	FTO/NiO_x/PVK(GN-GQDs)/PCBM/BCP/Ag	19.8%	90.1% of initial PCE, RH=30%, 30 days
Flexible n-i-p[11]	Fluoro graphene quantum dots (FGQDs)	PVK precursor additive	PEN/ITO/SnO_2/PVK/Spiro-OMeTAD/Ag	20.40 %	85% of initial PCE, 85 °C in N_2, 600 h
Flexible/Rigid p-i-n[12]	Graphene oxide (GO)	HTL	PEN(Glass)/ITO/GO/PVK/C60/Ag	9.34% (Flexible), 12.31 % (Rigid)	90% of initial PCE, ambient atmosphere, 120 h
Flexible p-i-n[13]	PATCVD-Graphene	PES/NiO_x Electrode	PES/Graphene/PVK/PCBM/AAA	14.2%	95% of initial PCE, 1000 bending cycles
Flexible/Rigid p-i-n[14]	GQDs	HTL	GR/GQDs/PVK/PCBM/Al	15.38 % (Flexible), 17.15 % (Rigid)	70% of initial PCE, 3000 bending cycles, 4 mm bending radius
Flexible p-i-n[15]	Graphene sheet of Cu grid-embedded polyimide (GCEP)	PI/ PEDOT:PSS hybrid electrode	GCEP/PEDOT:PSS/PVK/PCBM/ZnO/Ag	16.4%	95% of initial PCE, 1 sun illumination, 50 h
Flexible p-i-n[16]	Sulfonated graphene oxide (s-GO)	PVK precursor additive	PET/PEDOT:PSS/NiO_x/PVK:s-GO/PCBM/BCP/Ag	20.56 %	90% of initial PCE, ambient condition, 180 days
Flexible p-i-n (This work)	**Amino-functionalized graphene quantum dots (A-GQDs)**	**PVK/PCBM interface**	**PET/ITO/NiO_x/MeO-4PACz/PVK/A-GQDs/PCBM/BCP/Ag**	**23.11 %**	**81.3% of initial PCE, 1 sun illumination+85 °C in N_2, 1000 h**

Table S2. Performance parameters of reverse scan (RS) and forward scan (FS)

champion FPSCs of the control and A-GQDs FPSCs.

Type	A_1	τ_1 (ns)	A_2	τ_2 (ns)	τ_{ave} (ns)
Control	1.853	53.29	0.486	404.14	286.72
A-GQDs	0.957	80.59	0.544	779.43	671.59

Table S3. Statistical photovoltaic performance parameters of the control and A-GQDs FPSCs under the simulated solar illumination (AM 1.5G, 100 mW/cm^2, reverse scan).

Devices	V_{oc} (V)	J_{sc} (mA/cm^2)	FF (%)	PCE (%)
Control	1.104	23.21	78.37	20.08
	1.097±0.0029	23.12±0.08	76.52±1.78	19.41±0.55
A-GQDs	1.152	24.61	81.52	23.11
	1.152±0.0003	24.59±0.14	81.26±0.23	22.97±0.12

Table S4. Detailed photovoltaic parameters for the control and A-GQDs optimized flexible perovskite solar modules.

Devices	Scanning Direction	V_{oc} (V)	J_{sc} (mA/cm^2)	FF (%)	PCE (%)	HI (%)
Control	Reverse	6.349	3.87	73.34	18.02	7.88
	Forward	6.347	3.82	68.47	16.60	
A-GQDs	Reverse	6.466	4.09	76.56	20.24	2.07
	Forward	6.475	4.08	75.05	19.82	

Reference

[1] X. Ma, H. Luo, S. Jiang, L. Zheng, H. Xue, X. Li, Phase-Engineering of Layered Nickel Hydroxide for Synthesizing High-Quality NiO_x Nanocrystals for Efficient Inverted Flexible Perovskite Solar Cells, ACS Applied Materials & Interfaces, 15 (2023) 38444-38453.

[2] Q. Hu, K. Zhao, M. Liu, S. Riaz, Y. Qi, P. Wei, J. Cheng, Y. Xie, A dual passivation strategy based on F/N co-doped coal-based graphene quantum dots for high-efficiency carbon-based perovskite solar cells, Journal of Materials Chemistry A, 12 (2024) 5980-5989.

[3] Y. Zhou, S. Yang, X. Yin, J. Han, M. Tai, X. Zhao, H. Chen, Y. Gu, N. Wang, H. Lin, Enhancing electron transport via graphene quantum dot/SnO_2 composites for efficient and durable flexible perovskite photovoltaics, Journal of Materials Chemistry A, 7 (2019) 1878-1888.

[4] J. Xie, K. Huang, X. Yu, Z. Yang, K. Xiao, Y. Qiang, X. Zhu, L. Xu, P. Wang, C. Cui, D. Yang, Enhanced Electronic Properties of SnO_2 via Electron Transfer from Graphene Quantum Dots for Efficient Perovskite Solar Cells, ACS Nano, 11 (2017) 9176-9182.

[5] S. Pang, C. Zhang, H. Zhang, H. Dong, D. Chen, W. Zhu, H. Xi, J. Chang, Z. Lin, J. Zhang, Y. Hao, Boosting performance of perovskite solar cells with Graphene quantum dots decorated SnO2 electron transport layers, Applied Surface Science, 507 (2020) 145099.

[6] Z.-W. Gao, Y. Wang, H. Liu, J. Sun, J. Kim, Y. Li, B. Xu, W.C.H. Choy, Tailoring the Interface in $FAPbI_3$ Planar Perovskite Solar Cells by Imidazole-Graphene-Quantum-Dots, Advanced Functional Materials, 31 (2021) 2101438.

[7] Y. Chen, J. Chen, X. Wang, P. Deng, Y. Shen, X. Wang, Fluorinated graphene quantum dots-induced defect passivation of perovskite film toward stable and efficient perovskite solar cell, International Journal of Hydrogen Energy, 137 (2025) 107-113.

[8] G.-H. Kim, H. Jang, Y.J. Yoon, J. Jeong, S.Y. Park, B. Walker, I.-Y. Jeon, Y. Jo, H. Yoon, M. Kim, J.-B. Baek, D.S. Kim, J.Y. Kim, Fluorine Functionalized Graphene Nano Platelets for Highly Stable Inverted Perovskite Solar Cells, Nano Letters, 17 (2017) 6385-6390.

[9] F. Khan, M.T. Khan, S. Rehman, F. Al-Sulaiman, Analysis of electrical parameters of p-i-n perovskites solar cells during passivation via N-doped graphene quantum dots, Surfaces and Interfaces, 31 (2022) 102066.

[10] X. Gan, S. Yang, J. Zhang, G. Wang, P. He, H. Sun, H. Yuan, L. Yu, G. Ding, Y.

Zhu, Graphite-N Doped Graphene Quantum Dots as Semiconductor Additive in Perovskite Solar Cells, ACS Applied Materials & Interfaces, 11 (2019) 37796-37803.
[11] L. Yang, Y. Li, L. Wang, Y. Pei, Z. Wang, Y. Zhang, H. Lin, X. Li, Exfoliated Fluorographene Quantum Dots as Outstanding Passivants for Improved Flexible Perovskite Solar Cells, ACS Applied Materials & Interfaces, 12 (2020) 22992-23001.
[12] M.-A. Park, S.J. Sung, Y.J. Ahn, I. Hong, I.J. Park, C.R. Park, J.Y. Kim, Bifunctional Graphene Oxide Hole-Transporting and Barrier Layers for Transparent Bifacial Flexible Perovskite Solar Cells, ACS Applied Energy Materials, 4 (2021) 8824-8831.
[13] V.-D. Tran, S.V.N. Pammi, B.-J. Park, Y. Han, C. Jeon, S.-G. Yoon, Transfer-free graphene electrodes for super-flexible and semi-transparent perovskite solar cells fabricated under ambient air, Nano Energy, 65 (2019) 104018.
[14] S.H. Shin, D.H. Shin, S.-H. Choi, Enhancement of Stability of Inverted Flexible Perovskite Solar Cells by Employing Graphene-Quantum-Dots Hole Transport Layer and Graphene Transparent Electrode Codoped with Gold Nanoparticles and Bis(trifluoromethanesulfonyl)amide, ACS Sustainable Chemistry & Engineering, 7 (2019) 13178-13185.
[15] G. Jeong, D. Koo, J. Seo, S. Jung, Y. Choi, J. Lee, H. Park, Suppressed Interdiffusion and Degradation in Flexible and Transparent Metal Electrode-Based Perovskite Solar Cells with a Graphene Interlayer, Nano Letters, 20 (2020) 3718-3727.
[16] X. Hu, X. Meng, X. Yang, Z. Huang, Z. Xing, P. Li, L. Tan, M. Su, F. Li, Y. Chen, Y. Song, Cementitious grain-boundary passivation for flexible perovskite solar cells with superior environmental stability and mechanical robustness, Science Bulletin, 66 (2021) 527-535.